

## Article

# Novel Modelling Approach for Obtaining the Parameters of Low Ionosphere under Extreme Radiation in X-Spectral Range

Vladimir A. Srećković<sup>1,\*</sup>, Desanka M. Šulić<sup>2</sup>, Veljko Vujčić<sup>3</sup>, Zoran R. Mijić<sup>1</sup> and Ljubinko M. Ignjatović<sup>1</sup>

<sup>1</sup> Institute of Physics Belgrade, University of Belgrade, Pregrevica 118, 11080 Belgrade, Serbia; zoran.mijic@ipb.ac.rs (Z.R.M.); ljuba@ipb.ac.rs (L.M.I.)

<sup>2</sup> Faculty of Ecology and Environmental Protection, University Union—Nikola Tesla, 11000 Belgrade, Serbia; dsulic@unionnikolatesla.edu.rs

<sup>3</sup> Astronomical Observatory, Volgina 7, 11060 Belgrade, Serbia; veljko@aob.rs

\* Correspondence: vlada@ipb.ac.rs; Tel.: +381-(0)11-37-13-000

**Abstract:** Strong radiation from solar X-ray flares can produce increased ionization in the terrestrial D-region and change its structure. Moreover, extreme solar radiation in X-spectral range can create sudden ionospheric disturbances and can consequently affect devices on the terrain as well as signals from satellites and presumably cause numerous uncontrollable catastrophic events. One of the techniques for detection and analysis of solar flares is studying the variations in time of specific spectral lines. The aim of this work is to present our study of solar X-ray flare effects on D-region using very low-frequency radio signal measurements over a long path in parallel with the analysis of X-spectral radiation, and to obtain the atmospheric parameters (sharpness, reflection height, time delay). We introduce a novel modelling approach and give D-region coefficients needed for modelling this medium, as well as a simple expression for electron density of lower ionosphere plasmas. We provide the analysis and software on GitHub.

**Keywords:** solar radiation; sun activity; disturbances; radio spectra; X-spectral domain; Lyman-alpha



**Citation:** Srećković, V.A.; Šulić, D.M.; Vujčić, V.; Mijić, Z.R.; Ignjatović, L.M. Novel Modelling Approach for Obtaining the Parameters of Low Ionosphere under Extreme Radiation in X-Spectral Range. *Appl. Sci.* **2021**, *11*, 11574. <https://doi.org/10.3390/app112311574>

Academic Editor: Harry D. Kambezidis

Received: 20 October 2021  
Accepted: 1 December 2021  
Published: 6 December 2021

**Publisher's Note:** MDPI stays neutral with regard to jurisdictional claims in published maps and institutional affiliations.



**Copyright:** © 2021 by the authors. Licensee MDPI, Basel, Switzerland. This article is an open access article distributed under the terms and conditions of the Creative Commons Attribution (CC BY) license (<https://creativecommons.org/licenses/by/4.0/>).

## 1. Introduction

Solar flares (SFs) are giant eruptions on the surface of the Sun [1,2] that release huge amounts of electromagnetic energy over the whole electromagnetic spectrum [3–7]. Levels of photoionization processes in the ionosphere depend on plasma composition along with radiation spectral ranges at specific altitudes [8]. Information on certain solar spectral lines could be of importance in research of solar flares [9,10]. The enhanced Extreme Ultraviolet (EUV) radiation is absorbed at higher terrestrial altitudes additionally ionizing E and F regions of the ionosphere [11]. In addition, Lyman-alpha and X-rays penetrate more deeply into the ionosphere, reaching the D-region and causing enhanced ionization and absorption of electromagnetic (EM) waves there [12–14]. Solar flares can be classified into different classes based on their peak emission in the X-ray 0.1–0.8 nm spectral range as B ( $\geq 10^{-7} \text{ Wm}^{-2}$ ), C ( $\geq 10^{-6} \text{ Wm}^{-2}$ ), M ( $\geq 10^{-5} \text{ Wm}^{-2}$ ), and X ( $\geq 10^{-4} \text{ Wm}^{-2}$ ) classes [15–17].

The abrupt increase in X-radiation and EUV emission following solar flares causes additional ionization and increased absorption of EM waves in the sunlit part of the Earth's ionosphere. At the time of SFs and consequently during sudden ionospheric disturbances (SIDs), the gain of the atmosphere electron density at all heights is noticeable [18,19]. As a consequence of radiation influence, SFs create SIDs and induce disturbance in the monitored amplitude and phase of Very Low-Frequency (VLF in narrow band 3–30 kHz) radio signals, primarily in the D layer, which is located between the Earth's lower atmosphere, which has dense air, and its strongly conducting ionosphere [20,21]. These events of X-ray SFs have been monitored by Geostationary Operational Environmental Satellite (GOES) [15].

In this paper we will focus on the VLF technique—on amplitude and phase signals of worldwide transmitters of signals monitored by BEL VLF system (Belgrade, Serbia) [22]. VLF signals from the emitters located all over the world are continuously recorded by the BEL system. Events of X-ray SFs monitored by GOES satellites are further identified using a radio station's system of receivers. For these events, VLF wave enhancements are measured and analysed for the daytime atmosphere. In continuation of our previous research, the aim of this contribution is to present our study of solar X-ray flare effects and to obtain the daytime atmospheric parameters and ionization rate induced by this extreme radiation, and to provide a simple equation for altitude-dependent electron density of D-region plasma which depends on X-ray spectral intensity and sluggishness of the medium. Finally, we discuss how the approximately obtained altitude-dependent electron density relies on the shape of X-ray flux. The python scripts for calculating ionosphere parameters can be found on GitHub: <https://github.com/sambolino/flareD> (accessed on 17 October 2021).

The text is organized as follows: Section 2 briefly presents methods for observing the D-region and introduces a methodology. Section 3 provides the details of numerical results, analyses, and introduces a simple expression of electron density of the D-region. In Section 4 the results are discussed together with further directions of research.

## 2. SFs Impact

We have studied the VLF amplitude ( $A$ ) and phase ( $P$ ), acquired by recording VLF radio signals broadcast by NAA transmitter at Maine, USA ( $44.63^\circ$  N,  $67.28^\circ$  W) during solar-induced SIDs. The data were recorded by Belgrade VLF system ( $44.85^\circ$  N,  $20.38^\circ$  E). The BEL stations can synchronously record several radio signals broadcast by different transmitters. The technicalities and description of the BEL VLF system are presented in [22]. The NAA-BEL path is sufficiently long (6540 km) and correctly oriented west–east.

Here, we present the study of SIDs induced by the large SFs of solar cycles 24 and 25. The acquisition and research of VLF signals has been carried out together with the investigation of the corresponding X-ray fluxes obtained from GOES. In this research, the registered data of incoming solar radiation X-ray flux in the XRS spectral range of 0.1–0.8 nm are of primary interest.

### 2.1. Monitoring SF

We have studied the amplitude and phase data, obtained by monitoring VLF radio signals emitted by NAA/24.00 kHz transmitter during solar-induced SIDs. During SIDs, a regular method for signal examination and the determination of ionospheric parameters rely on the comparison between the registered variation of amplitude and phase and the matching values acquired with simulations by the Long-Wave Propagation Capability (LWPC) numerical software package [23,24], as explained in [20,25,26].

As an instructive example of a monitored active day, we present 7 September 2017 (see Figure 1). Three M-class solar flares erupted from sunspot AR2673 of magnitudes M2.4, M1.5, and M7.3, followed by a huge X1.3-class SF. Energy and particulates hurled at the Earth while the proton flux velocity was two times greater than normal. The aurora borealis was also seen.

In Figure 1 we present measured amplitude (lower panel) and phase (upper panel) for NAA/24.00 kHz signal on high solar activity during M1.5 ( $I_x = 1.5 \times 10^{-5}$ ,  $\text{Wm}^{-2}$  at peak time, 09:54 UT), M7.3 (10:15 UT), C3 (12:14 UT) and X1.3 (14:36 UT) events on 7 September 2017 as a function of time. There were visible changes in the VLF daily signal during the C, M and X flares (see signal peaks on panels). From Figure 1, one can see that these VLF and GOES peaks during the daytime happened almost simultaneously (with a time delay of the order of minutes).

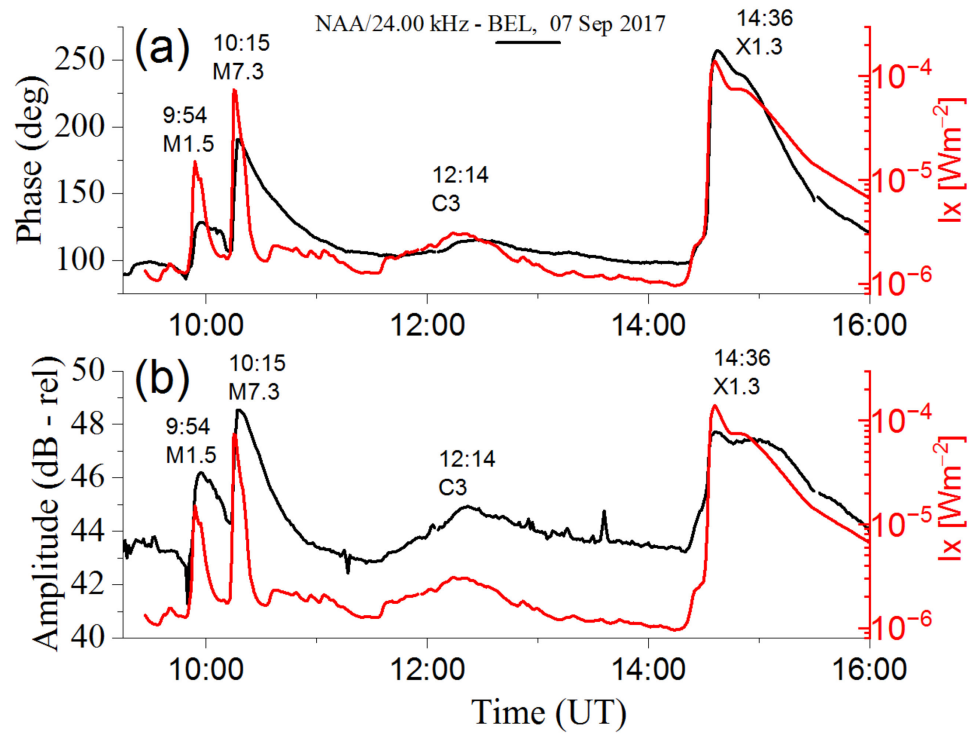


**Figure 1.** Time variation of X-ray irradiance on the right axes, NAA/24.00 kHz signal phase (a) and amplitude (b) during M1.5 (09:54 UT), M7.3 (10:15 UT), C3 (12:14 UT) and X1.3 (14:36 UT) events on 7 September 2017.

In this work we have calculated the amplitude increase  $\Delta A_{rec}$ , defined as the difference between the maximum amplitude  $A_{max}$  registered during the flare and the regular amplitude during quiet condition  $A_{quiet}$  as:

$$\Delta A_{rec} = A_{max} - A_{quiet} \tag{1}$$

In the same way, phase delay increase  $\Delta P_{rec}$  has been calculated as:

$$\Delta P_{rec} = P_{max} - P_{quiet} \tag{2}$$

The time delay  $\Delta t$  can be defined as:  $\Delta t = t_{Amax} - t_{I_{max}}$  where  $t_{Amax}$  is the time of maximum of VLF amplitude  $A_{max}$  and  $t_{I_{max}}$  is time of maximum of X-ray irradiance  $I_{max}$  [20]. The time delay is nearly similar to the D-region sluggishness [13] and is an important quantity that can be used to study the ionospheric response to the flares [27]. The quantity  $\Delta t$  depends on flare intensity and other factors, and usually takes values of about a few minutes [16,27].

For the representative quiet days, i.e., conditions, we have chosen the days under low solar activity. The conditions were that the daylight maximum of X-ray flux had to be lower than  $10^{-6} \text{ Wm}^{-2}$  in the 0.1–0.8 nm XL band.

## 2.2. Used Numerical Methods

### 2.2.1. Two-Component Exponential Model and Simulations

The daytime two-parameter exponential profile of electron density can be used for VLF modelling [28] and is given by:

$$N_e(h, H', \beta) = 1.43 \cdot 10^{13} \exp(-0.15 \cdot H') \exp[(\beta - 0.15) \cdot (h - H')] [\text{m}^{-3}]. \tag{3}$$

Here,  $\beta$  in  $\text{km}^{-1}$  is a time-dependent parameter of sharpness,  $H'$  is a reflection height in km, and  $h$  is the height in kilometres above surface.

During SIDs, a regular method for the obtaining of ionospheric parameters is based on comparison of the registered variation of amplitude and phase (Equations (1) and (2)) with the equal values obtained in computation by the LWPC software [23] as interpreted in [20,25,26].  $N_e$  can be obtained from the measured amplitude and phase changes by a trial-and-error method where density profile is modified until the LWPC computed amplitude and phase match with monitored data (see, e.g., [22]). Thus, the obtained parameters  $\beta$  and  $H'$  can be applied for further calculation and simulations (Equation (3), etc.).

### 2.2.2. FlarED' Method

In [29], i.e., GitHub: <https://github.com/sambolino/FlarED> (accessed on 17 October 2021), the database is created with SID VLF data ( $\Delta A_{rec}$ ,  $\Delta P_{rec}$ ) parameters, sharpness  $\beta$  and reflection height  $H'$  for different values of  $I_x$ , i.e., different classes of solar flares (during the period of ascending phase and maximum of the solar cycle 24 and 25). Solar flares are monitored and analysed by VLF technique and  $\Delta A_{rec}$ ,  $\Delta P_{rec}$  while parameters  $\beta$  and  $H'$  in database are obtained by the method described in [20]. The python scripts for calculating ionosphere parameters can be found <https://github.com/sambolino/FlarED> (accessed on 19 September 2021). For the input values of solar X-ray flux, parameters  $\beta$  and  $H'$  can be evaluated and altitude values of electron density for the low terrestrial ionosphere can be calculated. Users can easily calculate time series and height profile of electron density. The results, i.e., data, can be plotted and exported in csv.

### 2.2.3. Approximate Analytic Expression

In order to create an easier and more adequate use of results and data, we give an electron density specially modified simple logarithmic second-degree polynomial expression, with height-dependent coefficients taking into account the delay time of the ionosphere response. The python scripts for calculating electron density by this specially modified expression can be found at <https://github.com/sambolino/FlarED> (accessed on 10 October 2021). Additionally, for details see Section 3.2.

## 3. Results and Discussion

### 3.1. Analyses of SF Events

An example of flare-induced phase and amplitude perturbations, measured for the NAA/24.00 kHz signal on an active day of 10 May 2013, is given in Figure 2 (red lines on both panels). The unperturbed daytime values of phase and amplitude were measured on 9 May 2013 (black lines on both panels in Figure 2). There were visible changes in the VLF daily signal during the duration of M1.3 SF (peak time, 12:56 UT) and C2.5 SF (peak time, 14:37 UT).

One can see visible variations in amplitude and phase. SID VLF changes at the time of the maximum of SF of M1.3 and C2.5 SF classes are  $\Delta A = 4.2$  dB,  $\Delta P = 68.19$  deg and  $\Delta A = 1.06$  dB,  $\Delta P = 19.20$  deg, respectively (see Table 1 and Figure 3c,d). It can be seen that during SF class C, amplitude and phase disturbances are not well defined, but are still noticeable.

Figure 3 shows simultaneous variations of the sharpness  $\beta$ , effective reflection height  $H'$ , amplitude and phase (recorded and simulated), electron density at reference height (74 km) and X-ray flux, during the occurrence of two successive flares on 10 May 2013 from Figure 3a–e, respectively.

For the period around SFs on 10 May 2013, we have calculated the time-dependent  $H'$  and  $\beta$  parameters as shown in Figure 3a,b. During M1.3- and C2.5-class SFs on 10 May 2013, the change of  $H'$  with time has normal behaviour. After the start of the SFs it falls to a minimum, and after X-ray peak it keeps growing to a preflare value. Sharpness behaviour is connected with form of registered increase of VLF amplitude, i.e.,  $\beta$  rises sharply to a maximum, and after the peak of X-ray flux it drops to a preflare value. At 12:56 UT, i.e.,

at peak time of the M1.3-class SF, with  $I_x = 1.36 \cdot 10^{-5} \text{ Wm}^{-2}$ ,  $H'$  decreases to a value of 67 km and the  $\beta$  rises to  $0.41 \text{ km}^{-1}$ . At C2.5-class SF peak time (14:37 UT) with  $I_x = 2.59 \cdot 10^{-6} \text{ Wm}^{-2}$  the  $H'$  decreases to 72 km and the  $\beta$  increase to  $0.32 \text{ km}^{-1}$ . It can be noted that the reflection height and the sharpness are in correlation with X-ray flux shape.

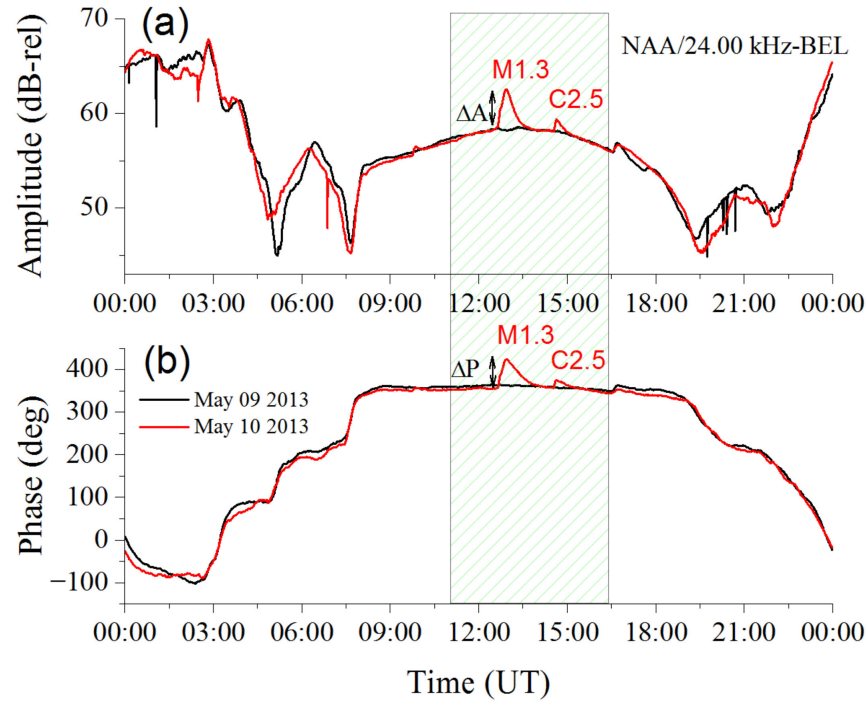


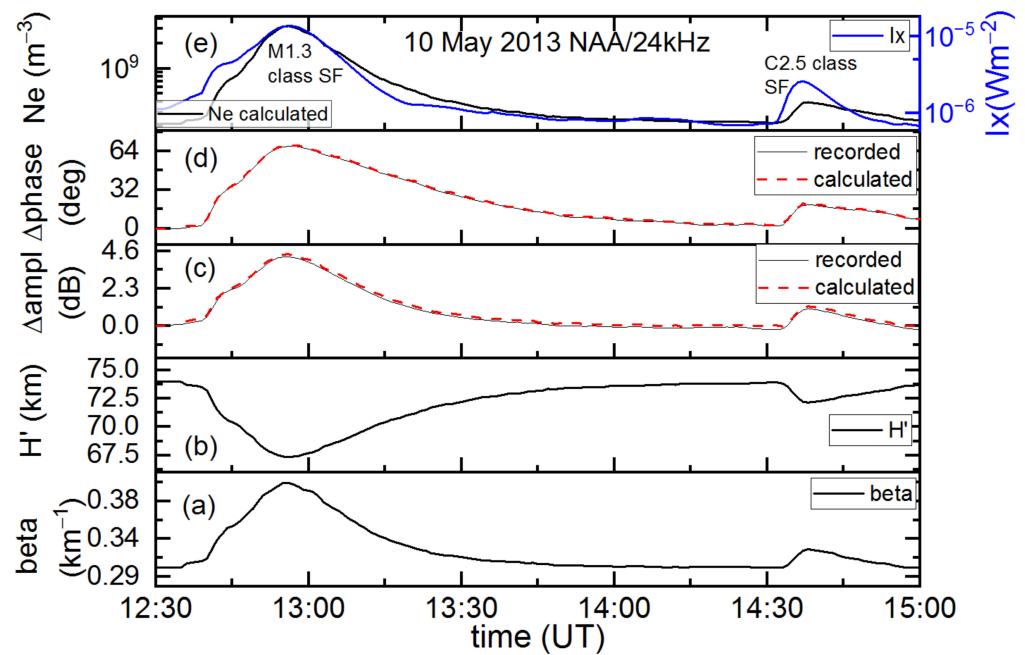
**Figure 2.** Measured variation of amplitude (a) and phase (b) on NAA signals for 9 May 2013 (quiet day) and 10 May 2013 with noticeable SF events.

**Table 1.** The data on SFs, amplitude and phase perturbations of VLF signals caused by different events analysed in this study.

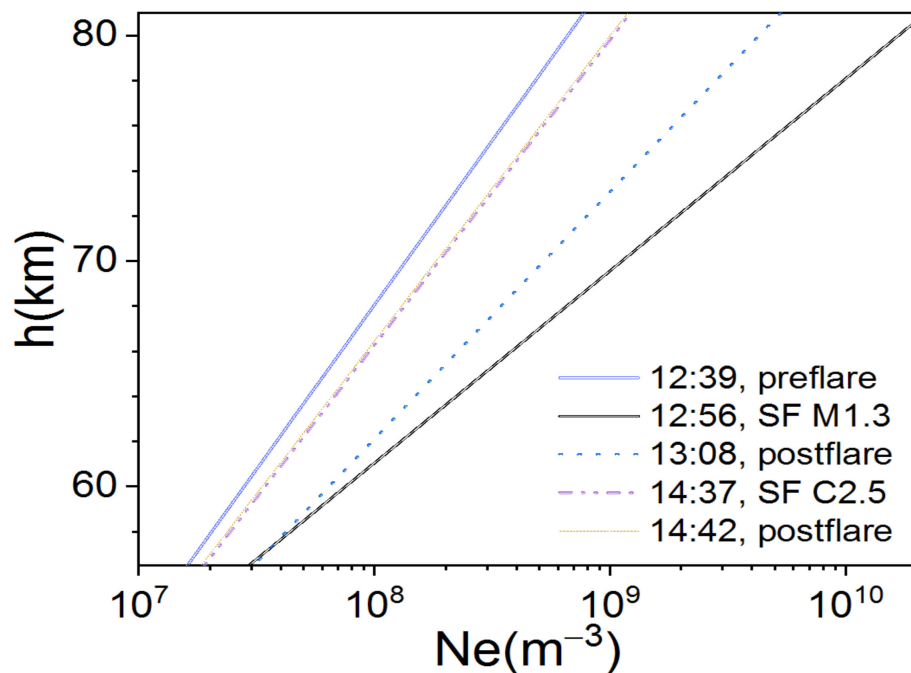
SF (Class, Date)	SF Tim			SID VLF Signatures			SF Data	
	Start [UT]	Peak [UT]	End [UT]	$\Delta A$ [dB]	$\Delta P$ [deg]	$\Delta t$ [min]	$I_x$ max XL [Wm <sup>-2</sup> ]	Active Region
M1.3 10.05.2013	12:37	12:56	13:04	4.20	68.19	0	$1.36 \times 10^{-5}$	1745
C2.5 10.05.2013	14:30	14:37	14:42	1.06	19.20	1	$2.59 \times 10^{-6}$	1745
M1.8 12.06.2014	09:23	09:37	09:42	4.50	51.47	4	$1.81 \times 10^{-5}$	2085
M2.7 12.06.2014	10:14	10:21	10:27	5.72	83.01	2	$2.74 \times 10^{-5}$	2087
X1.0 11.06.2014	08:59	09:06	09:10	5.54	90.45	3	$1.00 \times 10^{-4}$	2087
X1.3 07.09.2017	14:20	14:36	14:55	4.50	159	1	$1.39 \times 10^{-4}$	2673

Figure 4 shows the height profile, i.e., vertical electron-density profile before, after and during the M1.3- and C2.5-class solar flares that occurred on 10 May 2013. Electron-density altitude profile changes describe the variation of ionization at the D layer due to SF events and are relevant for mapping the low ionosphere [30,31] and moreover are important for checking the validity of the method and results [32] as shown in many examples. For unperturbed (preflare) ionospheric conditions (blue line) and post flare, there is a moderate increment in  $N_e$  (from  $2.8 \cdot 10^7 \text{ m}^{-3}$  at  $h = 60 \text{ km}$  height, to  $6.7 \cdot 10^8 \text{ m}^{-3}$  at the upper part of

this region, i.e., at  $h = 80$  km). These lines have almost the same behaviour. Completely different slope and behaviour have black and dashed dotted–dotted pink lines at peak times of M- and C-class SFs with increment from  $\sim 7 \cdot 10^7 \text{ m}^{-3}$  at 60 km height to  $1.6 \cdot 10^{10} \text{ m}^{-3}$  and  $4 \cdot 10^9 \text{ m}^{-3}$ , respectively. It can be noted that the electron density profiles moved to higher electron densities with different slopes when compared to the density profile of the preflare ionospheric condition. These changes in altitude profile of electron density are important for the nature of VLF propagation.



**Figure 3.** Simultaneous variations of the sharpness  $\beta$  (a), effective reflection height  $H'$  (b), VLF amplitude (c) and phase (d) excess recorded and simulated, electron density at reference height (e) and X-ray flux (on the right axis (e)) during the occurrence of two successive SFs on 10 May 2013.



**Figure 4.** The altitude profile of electron density during two successive SFs on 10 May 2013.

X-ray flux, amplitude, and phase of NAA/24.00 kHz radio signal as a function of UT during strong M-class successive SF on 12 June 2014 is presented in Figure 5. The lower panel shows perturbation of amplitude and X-ray flux, and in the upper panel perturbation of phase and X-ray flux is presented. We analysed two successive M-class solar flares (M1.8 with peak time 09:37 UT and M2.7 with peak time 10:21 UT). There were visible changes in the VLF daily signal during the duration of M1.8 SF and M2.7 SF. SID amplitude and phase changes at the peak time of SF of M1.8 and M2.7 SF classes are  $\Delta A = 4.5$  dB,  $\Delta P = 51.47$  deg and  $\Delta A = 5.72$  dB,  $\Delta P = 83.01$  deg, respectively (see Table 1 and Figure 6c,d).

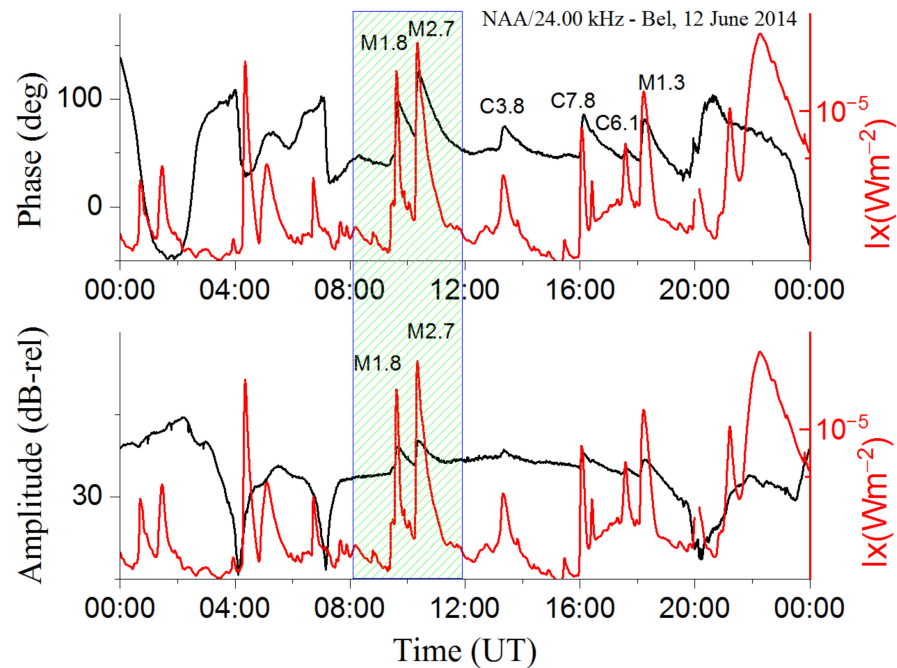


**Figure 5.** X-ray flux, amplitude, and phase of NAA signal during strong successive flares on 12 June 2014. (Lower panel) Amplitude and X-ray flux variation; (Upper panel) phase and X-ray flux variation.

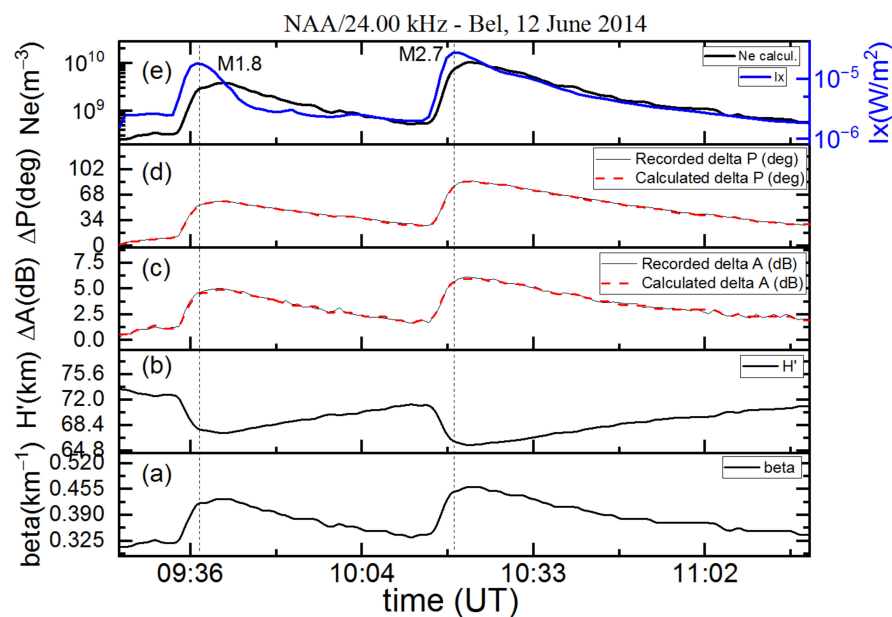


**Figure 6.** Variations of the sharpness  $\beta$  (a), effective reflection height  $H'$  (b), VLF amplitude (c) and phase (d) recorded and simulated, reference height electron density (e) and X-ray flux (on the right axis (e)), during the occurrence of two successive M-class SFs on 12 June 2014.

Sharpness  $\beta$ , effective reflection height  $H'$ , amplitude and phase of VLF signals (recorded and simulated), electron density at reference height, and X-ray flux during the presence of two M flares on 12 June 2014 are presented in Figure 6 on the upper to lower panels, respectively.

For the period around SF on 12 June 2014, we have calculated the time-dependent effective reflection height and sharpness as shown in Figure 6b,a. Generally, as in previous example, the shape of  $H'$  and  $\beta$  are in correlation with solar X-ray flux. During occurrences of M1.8- and M2.7-class SFs on 12 June 2014, the changes of  $H'$  during time have a normal nature.  $H'$  lowers in intensity to a minimum after SFs beginning and it rises to a preflare value after X-ray flux peaks. The structure of  $\beta$  is correlated with the amplitude shape. At the time of this SF, it rose quickly to a maximum after the SF peak time and then collapsed to preflare size. At peak time of the M1.8-class SF, ( $I_x = 1.81 \cdot 10^{-5} \text{ Wm}^{-2}$ ),  $H'$  lowers to a value of 67 km and  $\beta$  rises to  $0.42 \text{ km}^{-1}$ . At peak time 10:21 UT during M2.7-class SF with flux  $I_x = 2.7 \cdot 10^{-5} \text{ Wm}^{-2}$ , the  $H'$  decreases to 65 km and the sharpness increases to  $0.46 \text{ km}^{-1}$ .

The  $N_e$  at reference height is also in correlation with the intensity and shape of X-ray flux during the analysed time period (see Figure 6e).

Figure 7 presents the values of simulated amplitude and phase of the NAA signal along the GCP distance, obtained for quiet and disturbed ionospheric state during SFs on 12 June 2014. The simulations of propagation were performed using LWPC code. Amplitude and phase values of NAA signal proportionally increase with increasing X-ray intensity along the whole path. During the initial and main phase of the SID event, the signal variations are more frequent. SID events in the D-region are most noticeable as changes in the phase of VLF radio signals.

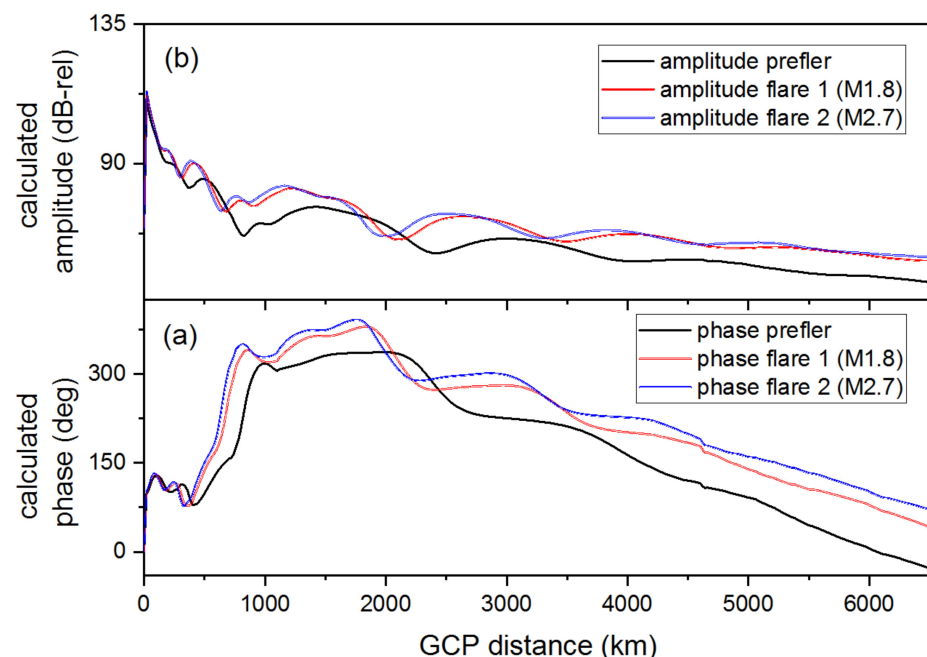


**Figure 7.** The phase (a) and amplitude (b) of the NAA/24.0 kHz signal along the GCP distance from Maine, USA, to BEL VLF station, Belgrade, obtained for quiet and disturbed ionospheric state during SFs on 12 June 2014.

The height profile, i.e., vertical  $N_e$  density profile before, after and during the M1.8- and M2.7-class solar flares on 12 June 2014 are shown in Figure 8. For unperturbed (preflare) conditions (black dashed line), one can see a slow increment of  $N_e$  (from  $3.2 \cdot 10^7 \text{ m}^{-3}$  at 60 km height, to about  $9.7 \cdot 10^8 \text{ m}^{-3}$  at 80 km height). Different slopes have a pink line and dashed red lines (at peak times of M-class SFs), with an increment from  $\sim 6 \cdot 10^7 \text{ m}^{-3}$  and  $\sim 1.2 \cdot 10^8 \text{ m}^{-3}$  at 60 km height to  $1.45 \cdot 10^{10} \text{ m}^{-3}$  and  $5 \cdot 10^{10} \text{ m}^{-3}$  at 80 km height, respectively.

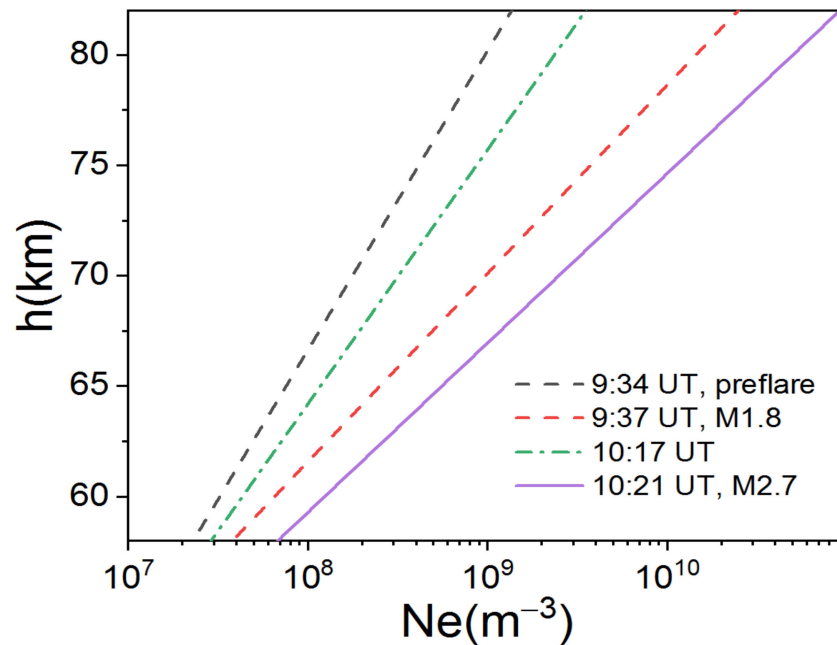


Figure 8. The altitude profile of electron density during two successive M-class SFs on 12 June 2014.

Strong SF: In order to cover the whole  $I_x$  spectral range needed for further analysis, we studied X-class solar flares with flux  $\geq 10^{-4} \text{ Wm}^{-2}$ . Figure 9 presents the values of the monitored and simulated excess of amplitude and phase of the NAA signal simultaneously with X-ray flux during SF on 11 June 2014. Measured and simulated signal values are in good agreement, i.e., almost identical. Barely visible differences are at the right corner of the figure, i.e., during relaxation time and the end of SF.

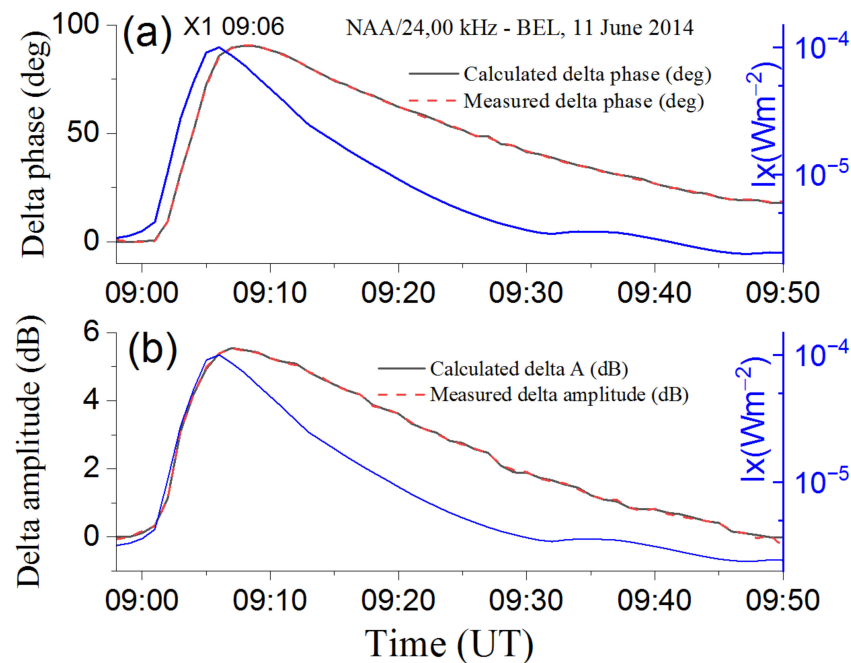
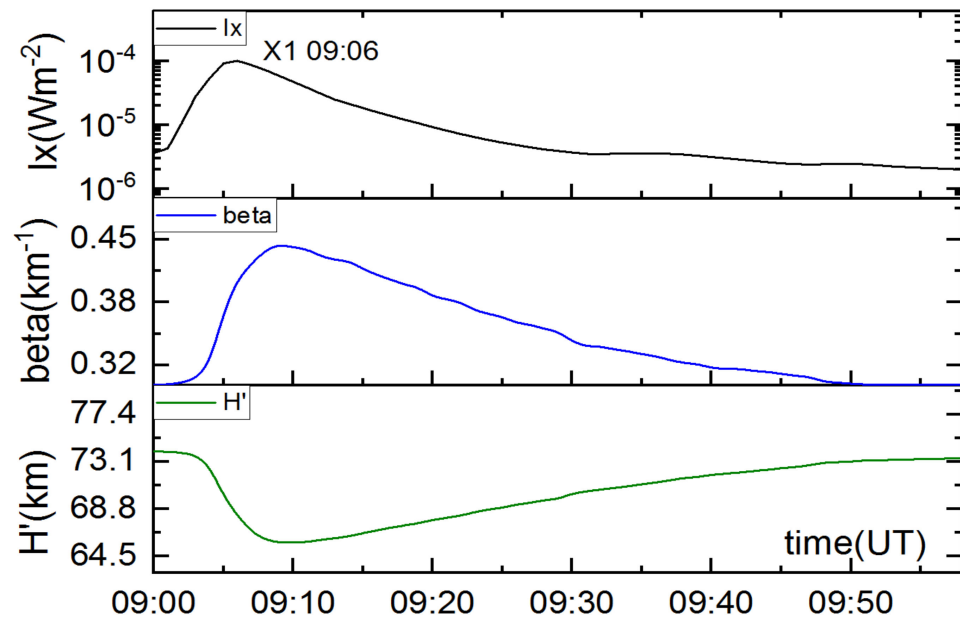


Figure 9. Time variation of X-ray irradiance (on the right axes), NAA/24.00 kHz signal phase (a) and amplitude (b) enhancement during M1.0 (09:06 UT) events on 11 June 2014.

Additionally, amplitude and phase values of NAA signal proportionally increase with increasing X-ray intensity, and during relaxation time (right wings of signal) amplitude

values decrease more slowly than the flux due to ionosphere sluggishness. For the period around SF on 11 June 2014, we have calculated the quantities needed for modelling such as the effective reflection height  $H'$  and the sharpness  $\beta$ , as shown in lower panels of Figure 10. One can see that the time profile, i.e., shape of reflection height and the sharpness are in correlation with X-ray flux. More precisely,  $\beta$  has almost the same form as  $I_x$  but shifted by  $\Delta t$ , while  $H'$  has a reverse shape.



**Figure 10.** Variations in the effective reflection height  $H'$ , sharpness  $\beta$  and X-ray irradiance during the occurrence of SF on 11 June 2014 are shown in panels from lower to upper, respectively.

### 3.2. Approximative Expressions and Simulations

Nowadays, more complicated methods and formulas exist and can be used in this field of science [27,33,34]. They are mostly related to calm conditions in the ionosphere, but still they are also used for perturbed conditions. However, the question arises of how easy some of them are for use and whether they are applicable when speed of analysis and obtaining products are important. The idea is to make the formula easy to use as well as to enable rapid calculations and analysis, such as for example the IRI model—the international standard empirical model for the terrestrial ionosphere [35,36].

In order to create an easier and more adequate use of the results and data, here we introduce the electron-density expression:

$$\log Ne(h, I_x(t), t + \Delta t) = \begin{cases} \sum_{i=0}^2 a_i(h) \cdot (\log(I_x^{\max}))^i, & t \leq t_{I_x^{\max}} \quad \text{a)} \\ y_0 + (2 * A / \pi i) * (w / (4 * (t - xc)^2 + w^2)), & t > t_{I_x^{\max}} \quad \text{b)} \end{cases} \quad (4)$$

where,  $t_{I_x^{\max}}$  is time of maximum of X-ray flux ( $\text{Wm}^{-2}$ ) and  $h$  is height (km),  $\Delta t$  is time delay defined earlier in the text and  $a_i(h)$  represents height-dependent dimensionless coefficients. Here,  $y_0 + (2 * A / \pi i) * (w / (4 * (t - xc)^2 + w^2))$  is Lorentzian function. Equation (4) gives more than satisfactory results when simplified (which was our intention to make it easy to use), i.e., when (4a) is valid for the whole time interval. Consequently, instead of whole Equation (4) we can use a simple logarithmic second-degree polynomial expression for the entire time interval, with height-dependent coefficients:

$$\log Ne(h, I_x(t), t + \Delta t) = \sum_{i=0}^2 a_i(h) \cdot (\log(I_x^{\max}))^i \quad (5)$$

Height-dependent coefficients  $a_i(h)$  can be found in the Github project. Compared to paper [37], here for the first time we introduce  $\Delta t$  and improve the expression by taking into account the delay time of the ionosphere response, making it more physical.

Time delay  $\Delta t$  in min can be presented (we use it further in the investigation) by linear dependence on the logarithm of X-ray flux (see, e.g., Figure 11)

$$\Delta t = \sum_{i=0}^1 c_i \cdot (\log(I_x^{\max}))^i \text{ [min]} \tag{6}$$

where dimensionless quantities take values  $c_0 = 0.45385$  and  $c_1 = -0.44863$  and  $I_x^{\max}$  is X-ray flux at peak time in  $[\text{Wm}^{-2}]$ . Further in the investigation we will use expression (6), which can be additionally corrected by inserting various influences. Of course, a more sophisticated formula might have been developed, but such precision was unnecessary since the values of the D-region parameters are known to fluctuate by an order of magnitude. The goal was to make the formula simple to use while also allowing for quick calculations and analysis.

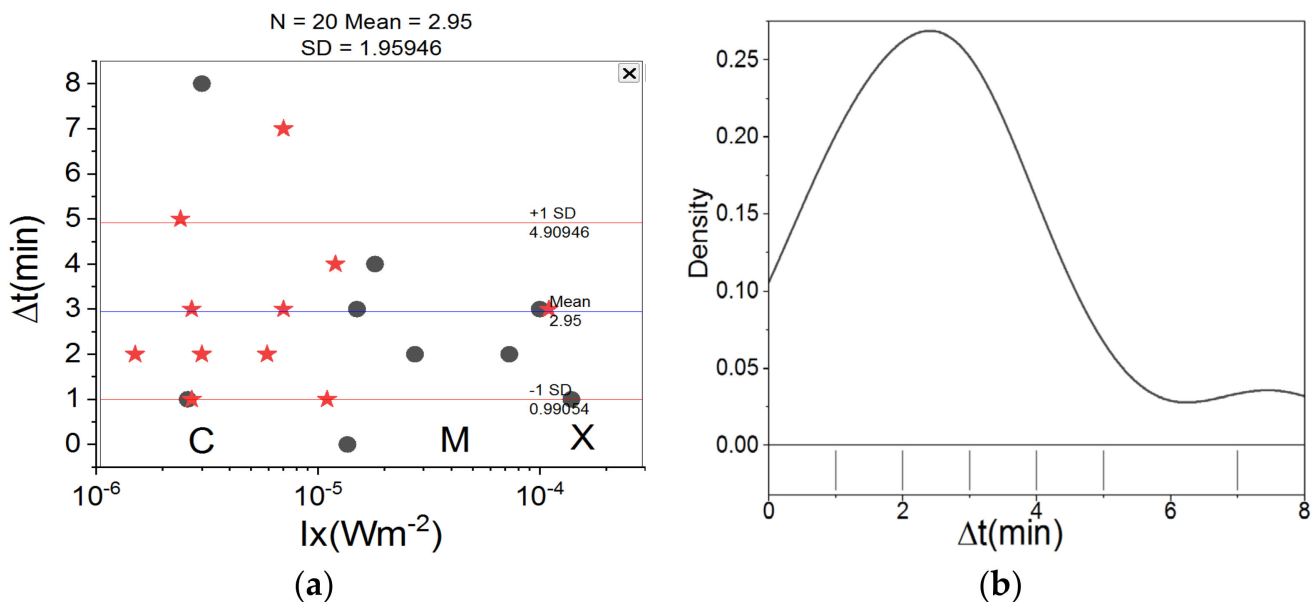


**Figure 11.** (a) The time delay  $\Delta t$  between the VLF amplitude max and the peak of SF X-ray flux as a function of peak flux (black circles are data from present investigation, red stars data from [27]); (b) Distribution of  $\Delta t$  data points (a rug plot).

In Figure 11a, we present values of obtained time delay  $\Delta t$  between the X-ray flux and the VLF amplitude as a function of peak flux. Black circles are data from present work and red stars are data from [27], obtained under the same conditions, i.e., with the same equipment and for the same transmitter–receiver path. Additionally, in Figure 11b we provide the distribution of  $\Delta t$  data points—a rug plot. The time delay between the X-ray flux and the VLF amplitude maximum  $\Delta t$  has a mean value of about 3 min. For C-class SFs,  $\Delta t$  is more scattered and has the highest variation, and for the larger values of flux  $I_x$  (M- and X-class SFs), the increase is the smallest.

From Figure 6 of the paper by Hayes et al. [38], one can see that presented data are scattered, even more so than in our case, with  $\Delta t$  up to 10 min and with a mean value of about two minutes, which is in accordance with our results. From Figure 11b (see rug plot), we certainly have the largest grouping between 1–4 min, which is also the case with the results of Hayes et al. [38] i.e., the results are in accordance. Certainly, there are other results in the literature such as from the paper of Basak & Chakrabarti [39], but our results and also the recent findings of Hayes et al. [38] differ from findings of Basak & Chakrabarti, which surely does not affect the main goal of the present work.

The conclusion is that the maximum of the signal, and consequently the electron density, is shifted by an average value of three minutes in relation to the maximum of the flux during the flare event due to ionosphere sluggishness. In addition, detailed statistics could have been performed but the main goal was to obtain a useful and easy to use expression for  $N_e$ .

Variation in X-ray flux (upper panel), measured by GOES-15, and  $N_e$  ( $h = 74$  km) as a function of UT during two successive flares on 12 June 2014 (lower panel) are presented in Figure 12. The red line in the lower panel shows results acquired by approximative Equation (5). The circles present values of electron density  $N_e$  obtained in this research by the method mentioned above using Equation (3). One can see that the results are in good agreement except the post-flare wings ( $N_e$  shape is more stretched). It can be noted that due to the sluggishness of the ionosphere, the shape of electron density over time does not totally follow the solar flux shape and it returns more slowly (post-flare wings) to a calm state due to the D-region relaxation time.

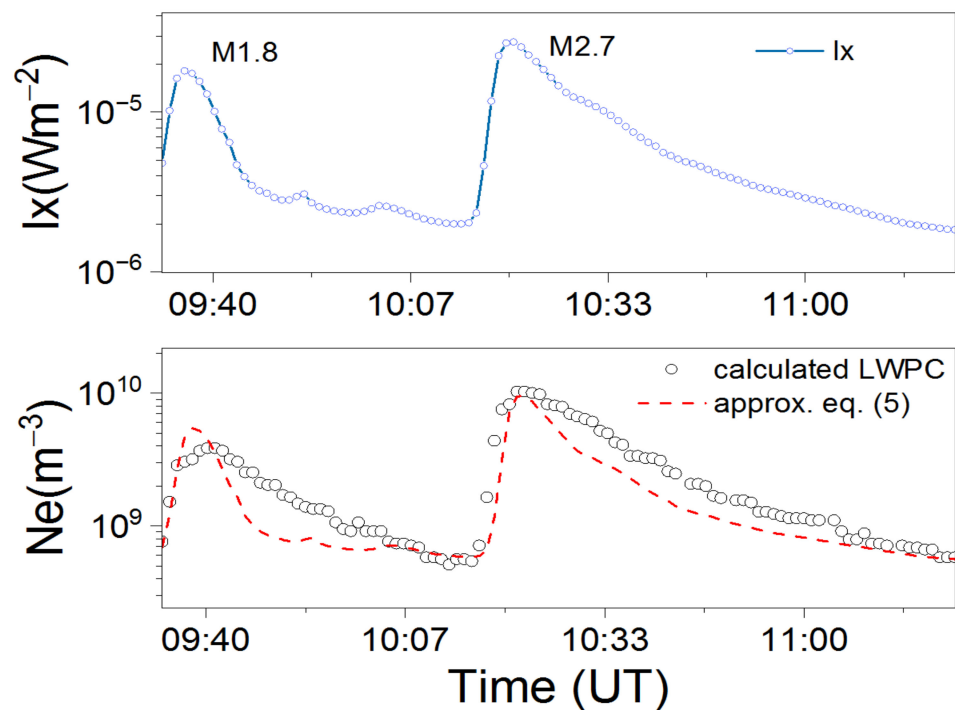


**Figure 12.** X-ray flux from GOES-15, and  $N_e$  ( $h = 74$  km) as a function of UT during two M-class SFs on 12 June 2014. The dashed red line shows results acquired by approximative Equation (5).  $N_e$  obtained by the above-mentioned method is presented by circles.

In [29], the database contains parameters  $\beta$  and  $H'$  for different values of  $I_x$ , i.e., different classes of solar flares (during the period of ascending phase and maximum of the solar cycle 24 and 25). Solar flares are monitored and analysed by VLF technique and parameters  $\beta$  and  $H'$  in database are obtained by method described in [20]. In <https://github.com/sambolino/flareD> (accessed on 19 September 2021) [29] for the input values of solar X-ray flux, Wait's parameters  $\beta$  and  $H'$  can be evaluated and altitude values of electron density for the low terrestrial ionosphere can be calculated.

Figure 13 presents a scatter plot of a pair of D-region parameters,  $H'$  and  $\beta$ , for SID cases analysed in this study together with data obtained using methods from [29]. Calculated parameters  $H'$  and  $\beta$  are in the range of 60–74 km and  $0.30$ – $0.60$   $\text{km}^{-1}$ , respectively. Black circles represent data from present work and red circles are related to the data obtained using the flared method (see Section 2.2.2). In the bottom right corner (for M- and X-classes of SF) data are more scattered.

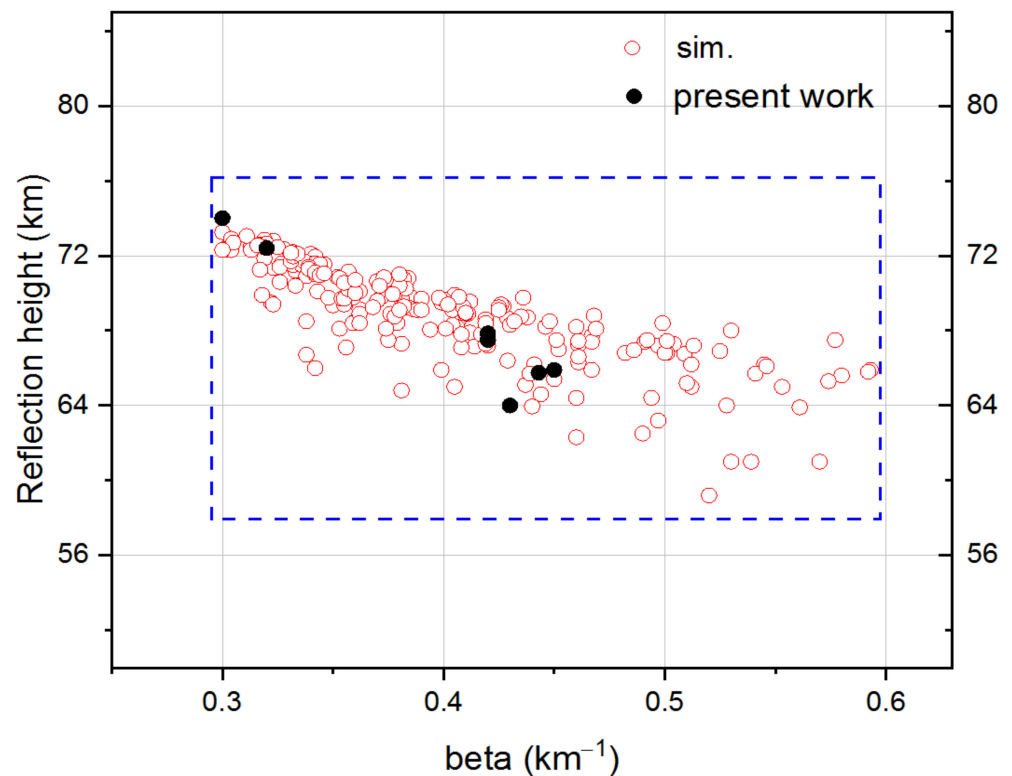


**Figure 13.** A scatter plot of a pair of D-region parameters, i.e.,  $H'$  versus  $\beta$ , is shown for SID cases analysed in this study using LWPC and two-component exponential model together with ones obtained using flared method from Github project [29].

### 3.3. Comparison of Results

In Figure 14, we present the results from this investigation, i.e., paper (using three methods from Sections 2.2.1–2.2.3), which are either simulated, calculated, approximated or the data obtained from literature [16,37,40–42], for electron density  $N_e$  at reference height as a function of X-ray flux. The area of importance is between the two red lines. It can be noticed that the results differ from each other in some cases by an order of magnitude or more. Although the data are scattered, especially for stronger flares (right side of the graph), they still tend to increase with the intensity of the X-ray radiation. As noted, our results were acquired on the basis of analysis of SID events on NAA/24.00 kHz signal and using methods described in the text. Electron density at reference height  $h = 74$  km changed from  $N_e = 2.16 \times 10^8 \text{ m}^{-3}$  to  $N_e > 10^{11} \text{ m}^{-3}$ . Additionally, we compared data with the  $N_e$  data obtained using approximate Equation (5) (plus sign in Figure 14) and simulations (black star) using the flared method. The results are in fair agreement with previous studies. We can conclude that measurements over a long path give slightly higher slope, i.e., lower values of electron density than expected, but are quite satisfactory. This is important because most results concerning investigation in the D-region are scattered and vary in order of magnitude and we need to take into account all the data and correct the existing ones. During SIDs the time profile of electron density follows the solar X-ray flux variation.

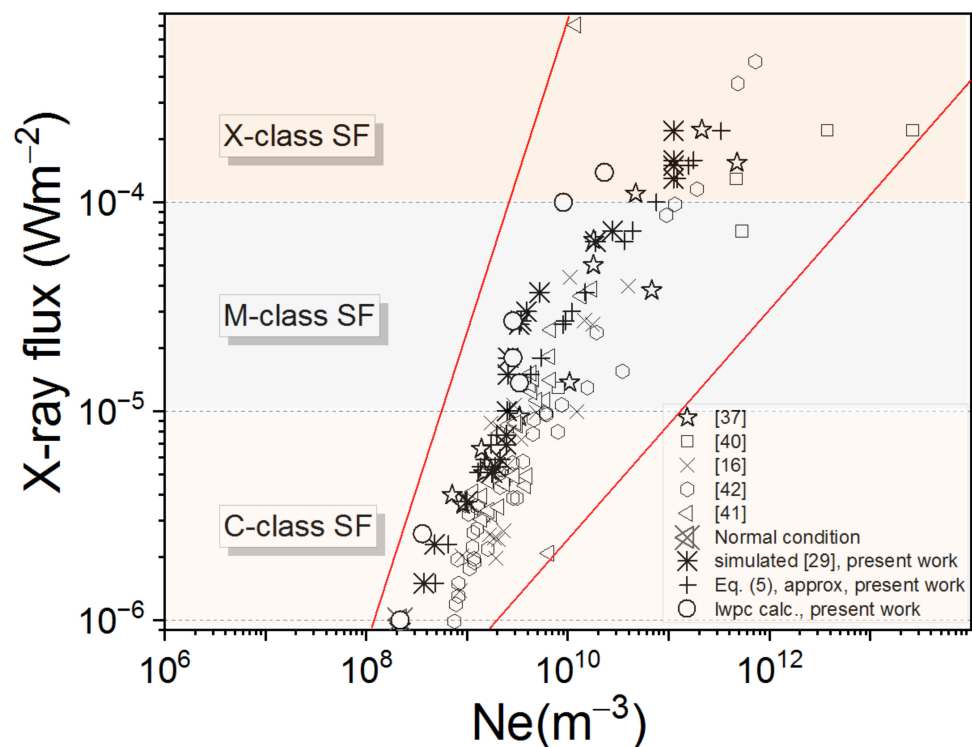


**Figure 14.** Electron-density data (calculated, simulated and approximated) at reference height  $h = 74$  km and maximum of  $I_x$  flux during occurrence of different class SFs. The data are compared with results from [16,37,40–42]. Area of importance is between the two red lines.

#### 4. Conclusions and Perspectives

In this paper we analysed SF events with extreme radiation in the X-spectral range. The perturbed VLF data were collected by monitoring the NAA/24.00 kHz VLF signal (transmitted in Maine, USA and then received in Belgrade, with GCP = 6540 km) and used together with GOES satellite data. The magnitude of impact of SFs on D-region and the consequences of these explosive events were analysed using measurements over a long path. The amplitude and phase data and ionosphere parameters during the enhancements of radiation due to the SF obtained in our study, are presented.

The GCP from the NAA transmitter to the Belgrade receiver is about 6540 km long and characterized as a long, dominantly sea path, and we studied cases when it is entirely sunlit. The data obtained here demonstrate the advantages of using these long-path measurements due to stable form of phase and amplitude variation caused by SID in contrast to the VLF perturbations on the short path which display more complexity and oscillations, including decreases and increases depending on the flare intensity. This is very important during the modelling process.

Furthermore, we conclude that the intensity of amplitude and phase perturbations on VLF kHz signal over a long path is in correlation with the size and shape of X-ray flux. This is in line with previous studies. The most effective influence on the enhancement of the ionization rate in the D-region during the observed SFs is due to the increased intensity of spectral lines in the X-ray spectra. Moreover, X-ray SFs with larger line intensities produce a larger increase in electron density. The computation was applied, and we obtained coefficients, i.e., sharpness, reflection height, and time delay needed for modelling this medium under increased radiation in the X-spectral range. One can notice that the intensified solar radiation in the X-spectral range changes D-region parameters and conducts an enhanced production rate, consequently deforming the VLF signal. The dependence of electron density on X-ray flux has slightly lower slope but is in fair agreement with previous studies.

The present manuscript offers an extension of the electron-density modeling in the daytime, SF-perturbed D-region of the ionosphere already introduced in [37]. In particular, the extension includes time delays from ionospheric sluggishness in  $N_e$  modeling, making use of data over a long GC path that ensures enhanced stability of SID-induced variations in phase and amplitude shape. The construction of the associated flarED GitHub project is designed to be easily applicable.

Moreover, we introduce novel methods and provide a simple, modified expression for  $N_e$  as a function of  $I_x$ , valid for unperturbed and perturbed conditions. We develop the expression by taking into account the delay time of the ionosphere response, making it more physical. The analysis and software are provided on GitHub under the MIT license.

In addition, the observed increase in the atmospheric aerosol number density after the event of SFs in February and March 2011, as well as high-level cloud formation in the upper atmosphere, reveal the importance of further investigation of SF and possible influence on particle-electrification mechanisms [43–45]. Recent studies [46] have introduced reconsideration of atmospheric aerosol–electricity interactions, which could improve theoretical understanding and simulations of the aerosol lifecycle, opening new horizons for weather and climate science. Future research will focus on a multidiscipline approach, investigating solar–geomagnetic activity effects on aerosol particles and on radiative transfer.

**Author Contributions:** Conceptualization, V.A.S. and D.M.Š.; writing—original draft preparation, V.A.S., Z.R.M.; writing—review and editing, V.A.S., D.M.Š., V.V., Z.R.M.; supervision, L.M.I. All authors have read and agreed to the published version of the manuscript.

**Funding:** This work was funded by the Institute of Physics Belgrade and University Union—Nikola Tesla Belgrade, through a grant by the Ministry of Education and Science of the Republic of Serbia. This article/publication is based upon work from COST Action CA17126—Towards understanding and modelling intense electronic excitation (TUMIEE), supported by COST (European Cooperation in Science and Technology).

**Institutional Review Board Statement:** Not applicable.

**Informed Consent Statement:** Not applicable.

**Data Availability Statement:** New dataset from this study is publicly available as well as python functions for calculating ionosphere parameters on GitHub: <https://github.com/sambolino/flarED> (accessed on 10 October 2021). Publicly available datasets were analysed in this study and can be found at <https://satdat.ngdc.noaa.gov/sem/goes/data/avg> (accessed on 2 September 2021).

**Acknowledgments:** We would like to express our appreciation to Ognyan Kounchev and Magdalena Christova for the shown attention to this paper and for a fruitful dialogue.

**Conflicts of Interest:** The authors declare no conflict of interest. The funders had no role in the design of the study; in the collection, analyses, or interpretation of data; in the writing of the manuscript, or in the decision to publish the results.

## References

1. Bothmer, V.; Daglis, I.A. *Space Weather: Physics and Effects*; Springer Science & Business Media: Berlin/Heidelberg, Germany, 2007.
2. Smith, H.J.; Smith, E.V.P. *Solar Flares*; Macmillan: New York, NY, USA, 1963.
3. Davidson, B. *Weatherman's Guide to the Sun*, 3rd ed.; Space Weather News, LLC.: New York, NY, USA, 2020.
4. Doschek, G.; Meekins, J.; Cowan, R.D. Spectra of solar flares from 8.5 Å to 16 Å. *Sol. Phys.* **1973**, *29*, 125–141. [[CrossRef](#)]
5. Tandberg-Hanssen, E.; Emslie, A.G. *The Physics of Solar Flares*; Cambridge University Press: Cambridge, UK, 2009.
6. Reames, D.V.; Murdin, P. Solar Wind: Energetic Particles. *Encycl. Astron. Astrophys.* **2002**, *2312*, 1–122.
7. Tandon, J.; Deshpande, S.; Bhatia, V. Electromagnetic radiation from solar flares. *Nature* **1968**, *220*, 1213–1214. [[CrossRef](#)]
8. Basseur, G.P.; Solomon, S. Composition and chemistry. In *Aeronomy of the Middle Atmosphere: Chemistry and Physics of the Stratosphere and Mesosphere*; Springer: Berlin/Heidelberg, Germany, 2005; pp. 265–442.
9. Nina, A.; Čadež, V.; Srećković, V.; Šulić, D. The influence of solar spectral lines on electron concentration in terrestrial ionosphere. *Open Astron.* **2011**, *20*, 609–612. [[CrossRef](#)]
10. Valnicek, B.; Ranzinger, P. X-ray emission and D-region “sluggishness”. *Bull. Astron. Inst. Czechoslov.* **1972**, *23*, 318.
11. Bain, W.C.; Hammond, E. Ionospheric solar flare effect observations. *J. Atmos. Sol. Terr. Phys.* **1975**, *37*, 573–574. [[CrossRef](#)]

12. Brasseur, G.P.; Solomon, S. Radiation. In *Aeronomy of the Middle Atmosphere: Chemistry and Physics of the Stratosphere and Mesosphere*; Springer: Berlin/Heidelberg, Germany, 2005; pp. 151–264.
13. Mitra, A.P. *Ionospheric Effects of Solar Flares*; Springer: Berlin/Heidelberg, The Netherlands, 1974. [CrossRef]
14. Nicolet, M.; Swider, W., Jr. Ionospheric conditions. *Planet. Space Sci.* **1963**, *11*, 1459–1482. [CrossRef]
15. Garcia, H.A. Temperature and emission measure from GOES soft X-ray measurements. *Sol. Phys.* **1994**, *154*, 275–308. [CrossRef]
16. Grubor, D.; Šulić, D.; Žigman, V. Classification of X-ray solar flares regarding their effects on the lower ionosphere electron density profile. *Ann. Geophys.* **2008**, *26*, 1731–1740. [CrossRef]
17. Wang, X.; Chen, Y.; Toth, G.; Manchester, W.B.; Gombosi, T.I.; Hero, A.O.; Jiao, Z.; Sun, H.; Jin, M.; Liu, Y. Predicting solar flares with machine learning: Investigating solar cycle dependence. *Astrophys. J.* **2020**, *895*, 3. [CrossRef]
18. Kelley, M.C. *The Earth's Ionosphere: Plasma Physics and Electrodynamics*, ser. *International Geophysics*, 2nd ed.; Academic Press: Cambridge, MA, USA, 2009.
19. Wah, W.P.; Abdullah, M.; Hasbi, A.M.; Bahari, S.A. Development of a VLF receiver system for sudden ionospheric disturbances (SID) detection. In Proceedings of the 2012 IEEE Asia-Pacific Conference on Applied Electromagnetics (APACE), Melaka, Malaysia, 11–13 December; pp. 98–103.
20. Šulić, D.; Srećković, V.; Mihajlov, A. A study of VLF signals variations associated with the changes of ionization level in the D-region in consequence of solar conditions. *Adv. Space Res.* **2016**, *57*, 1029–1043. [CrossRef]
21. Volland, H. On the solar flare effect of vlf-waves in the lower ionosphere. *J. Atmos. Sol.-Terr. Phys.* **1964**, *26*, 695–709. [CrossRef]
22. Šulić, D.; Srećković, V. A comparative study of measured amplitude and phase perturbations of VLF and LF radio signals induced by solar flares. *Serb. Astron. J.* **2014**, *188*, 45–54. [CrossRef]
23. Ferguson, A.J. *Computer Programs for Assessment of Long-Wavelength Radio Communications, Version 2.0: User's Guide and Source Files*; Space and Naval Warfare Systems Center: San Diego, CA, USA, 1998.
24. LWPC. Computer Programs for Assessment of Long-Wavelength Radio Communications, V2.1. 2018. Available online: <https://github.com/space-physics/LWPC> (accessed on 30 June 2021).
25. Nina, A.; Čadež, V.; Srećković, V.; Šulić, D. Altitude distribution of electron concentration in ionospheric D-region in presence of time-varying solar radiation flux. *Nucl. Instrum. Methods Phys. Res. B* **2012**, *279*, 110–113. [CrossRef]
26. Nina, A.; Čadež, V.; Šulić, D.; Srećković, V.; Žigman, V. Effective electron recombination coefficient in ionospheric D-region during the relaxation regime after solar flare from February 18, 2011. *Nucl. Instrum. Methods Phys. Res. B* **2012**, *279*, 106–109. [CrossRef]
27. Žigman, V.; Grubor, D.; Šulić, D. D-region electron density evaluated from VLF amplitude time delay during X-ray solar flares. *J. Atmos. Sol.-Terr. Phys.* **2007**, *69*, 775–792. [CrossRef]
28. Wait, J.R.; Spies, K.P. *Characteristics of the Earth-Ionosphere Waveguide for VLF Radio Waves, Technical Note 300*; US Department of Commerce, National Bureau of Standards: Boulder, CO, USA, 1964.
29. Vujčić, V.; Srećković, V.A. flarED Flare Electron Density. Available online: <https://github.com/sambolino/flarED> (accessed on 19 September 2021).
30. Da Silva, C.L.; Salazar, S.D.; Brum, C.G.; Terra, P. Survey of electron density changes in the daytime ionosphere over the Arecibo observatory due to lightning and solar flares. *Sci. Rep.* **2021**, *11*, 1–12. [CrossRef]
31. Kolarski, A.; Grubor, D. Sensing the Earth's low ionosphere during solar flares using VLF signals and goes solar X-ray data. *Adv. Space Res.* **2014**, *53*, 1595–1602. [CrossRef]
32. Kolarski, A.; Grubor, D. Comparative analysis of VLF signal variation along trajectory induced by X-ray solar flares. *J. Astrophys. Astron.* **2015**, *36*, 565–579. [CrossRef]
33. Nina, A.; Nico, G.; Mitrović, S.T.; Čadež, V.M.; Milošević, I.R.; Radovanović, M.; Popović, L.Č. Quiet Ionospheric D-Region (QIonDR) Model Based on VLF/LF Observations. *Remote Sens.* **2021**, *13*, 483. [CrossRef]
34. Palit, S.; Basak, T.; Mondal, S.; Pal, S.; Chakrabarti, S. Modeling of very low frequency (VLF) radio wave signal profile due to solar flares using the GEANT4 Monte Carlo simulation coupled with ionospheric chemistry. *Atmos. Chem. Phys.* **2013**, *13*, 9159–9168. [CrossRef]
35. Sezen, U.; Gulyaeva, T.L.; Arıkan, F. Online international reference ionosphere extended to plasmasphere (IRI-Plas) model. In Proceedings of the 2017 XXXIInd General Assembly and Scientific Symposium of the International Union of Radio Science (URSI GASS), Montreal, QC, Canada, 19–26 August 2017; pp. 1–4.
36. Bilitza, D.; Altadill, D.; Truhlik, V.; Shubin, V.; Galkin, I.; Reinisch, B.; Huang, X. International Reference Ionosphere 2016: From Ionospheric Climate to Real-Time Weather Predictions. *Space Weather.* **2017**, *15*, 418–429. [CrossRef]
37. Srećković, V.A.; Šulić, D.M.; Ignjatović, L.; Vujčić, V. Low Ionosphere under Influence of Strong Solar Radiation: Diagnostics and Modeling. *Appl. Sci.* **2021**, *11*, 7194. [CrossRef]
38. Hayes, L.A.; O'Hara, O.S.; Murray, S.A.; Gallagher, P.T. Solar Flare Effects on the Earth's Lower Ionosphere. *Sol. Phys.* **2021**, *296*, 1–17. [CrossRef]
39. Basak, T.; Chakrabarti, S.K. Effective recombination coefficient and solar zenith angle effects on low-latitude D-region ionosphere evaluated from VLF signal amplitude and its time delay during X-ray solar flares. *Astrophys. Space Sci.* **2013**, *348*, 315–326. [CrossRef]
40. Gavrilov, B.; Ermak, V.; Lyakhov, A.; Poklad, Y.V.; Rybakov, V.; Ryakhovsky, I. Reconstruction of the Parameters of the Lower Midlatitude Ionosphere in M-and X-Class Solar Flares. *Geomagn. Aeron.* **2020**, *60*, 747–753. [CrossRef]

41. Pandey, U.; Singh, B.; Singh, O.; Saraswat, V. Solar flare induced ionospheric D-region perturbation as observed at a low latitude station Agra, India. *Astrophys. Space Sci.* **2015**, *357*, 1–11. [[CrossRef](#)]
42. Thomson, N.R.; Clilverd, M.A. Solar flare induced ionospheric D-region enhancements from VLF amplitude observations. *J. Atmos. Sol.-Terr. Phys.* **2001**, *63*, 1729–1737. [[CrossRef](#)]
43. Avakyan, S. Supramolecular physics of the solar-troposphere links: Control of the cloud cover by solar flares and geomagnetic storms. In Proceedings of the 11th Intl School and Conference “Problems of Geocosmos”, St. Petersburg, Russia, 3–7 October 2016; pp. 187–191.
44. Goncharenko, Y.V.; Kivva, F. Evaluation of Size of the Atmospheric Aerosol Particles in the Reflecting Layers Occurring after Intense Solar Flares. *Telecommun. Radio Eng.* **2003**, *59*, 1–6.
45. McGrath-Spangler, E.L.; Denning, A.S. Global seasonal variations of midday planetary boundary layer depth from CALIPSO space-borne LIDAR. *J. Geophys. Res.* **2013**, *118*, 1226–1233. [[CrossRef](#)]
46. Mallios, S.A.; Daskalopoulou, V.; Amiridis, V. Orientation of non spherical prolate dust particles moving vertically in the Earth’s atmosphere. *J. Aerosol. Sci.* **2021**, *151*, 105657. [[CrossRef](#)]